

DISK AND ENVELOPE STRUCTURE IN CLASS 0 PROTOSTARS. I. THE RESOLVED MASSIVE DISK IN SERPENS FIRS 1

MELISSA L. ENOCH^{1,5}, STUART CORDER^{2,6}, MICHAEL M. DUNHAM³, AND GASPARD DUCHÊNE^{1,4}¹ Department of Astronomy, University of California at Berkeley, 601 Campbell Hall, Berkeley, CA 94720, USA; menoch@berkeley.edu² NRAO/ALMA-JAO, Av. Apoquindo 3650, Piso 18, Las Condes, Santiago, Chile³ Department of Astronomy, The University of Texas at Austin, 1 University Station, C1400, Austin, TX 78712, USA⁴ Université Joseph Fourier-Grenoble 1/CNRS, Laboratoire d'Astrophysique de Grenoble (LAOG) UMR 5571, BP 53, 38041 Grenoble Cedex 09, France

Received 2009 August 4; accepted 2009 October 19; published 2009 November 18

ABSTRACT

We present the first results of a program to characterize the disk and envelope structure of typical Class 0 protostars in nearby low-mass star-forming regions. We use *Spitzer* Infrared Spectrograph (IRS) mid-infrared spectra, high-resolution Combined Array for Research in Millimeter-wave Astronomy (CARMA) 230 GHz continuum imaging, and two-dimensional radiative transfer models to constrain the envelope structure, as well as the size and mass of the circumprotostellar disk in Serpens FIRS 1. The primary envelope parameters (centrifugal radius, outer radius, outflow opening angle, and inclination) are well constrained by the spectral energy distribution (SED), including *Spitzer* IRAC and MIPS photometry, IRS spectra, and 1.1 mm Bolocam photometry. These together with the excellent *uv*-coverage (4.5–500 k λ) of multiple antenna configurations with CARMA allow for a robust separation of the envelope and a resolved disk. The SED of Serpens FIRS 1 is best fit by an envelope with the density profile of a rotating, collapsing spheroid with an inner (centrifugal) radius of approximately 600 AU, and the millimeter data by a large resolved disk with $M_{\text{disk}} \sim 1.0 M_{\odot}$ and $R_{\text{disk}} \sim 300$ AU. These results suggest that large, massive disks can be present early in the main accretion phase. Results for the larger, unbiased sample of Class 0 sources in the Perseus, Serpens, and Ophiuchus molecular clouds are needed to determine if relatively massive disks are typical in the Class 0 stage.

Key words: infrared: ISM – ISM: individual (Serpens) – stars: formation – submillimeter

Online-only material: color figures, machine-readable table

1. INTRODUCTION

Protostars build up their mass by accreting material from a dense protostellar envelope, presumably via a rotationally supported circumprotostellar accretion disk. Disk formation is a natural result of collapse in a rotating core, but it is not known how soon after protostellar formation the disk appears, or how massive it is at early times. Theory suggests that centrifugally supported disks should start out small (radius less than 10 AU), and thus low mass, and grow with time (Terebey et al. 1984). Unstable or magnetically supported disks, however, could be much larger (radii up to 1000 AU in the magnetically supported case; Galli & Shu 1993), and thus more massive at early times.

The remnants of these protostellar accretion disks are easily observed in more evolved phases (e.g., T Tauri stars), but given that the majority of mass is accreted during earlier embedded phases, understanding disks at early times is critical. Directly observing disks during this main accretion phase is quite difficult, however, as they are hidden within dense, extinguishing protostellar envelopes. The structure of the envelope at small radii is another important characteristic of main accretion phase protostars that is similarly difficult to directly observe. Disk growth or the presence of a binary companion may clear out the inner region of the envelope early on, as inferred for the binary Class 0 source IRAS 16293–2422 by Jørgensen et al. (2005b).

There has been a recent push toward detecting disks in more embedded objects, with many now known and roughly characterized in Class I protostars (e.g., Looney et al. 2000;

Jørgensen et al. 2005a; Eisner et al. 2005; Andrews & Williams 2007), and a few detected in the earlier Class 0 stage (e.g., Chandler et al. 1995; Harvey et al. 2003; Brown et al. 2000; Looney et al. 2000).⁷ Most previous detailed studies have been limited to the most well known or brightest Class 0 sources, however, due to instrumental limitations and a lack of large unbiased target samples. The ongoing Submillimeter Array survey of low-mass protostars (Jørgensen et al. 2007, 2009) is a notable exception.

With recent large surveys of nearby molecular clouds at mid-infrared and (sub)millimeter wavelengths, it is now possible to define complete samples of Class 0 protostars based on luminosity or envelope mass limits (e.g., Hatchell et al. 2007; Jørgensen et al. 2008; Dunham et al. 2008; Enoch et al. 2009; Evans et al. 2009).

We have recently begun a campaign to characterize disk properties in a large, uniform sample of Class 0 protostars in nearby low mass star-forming regions (M. Enoch et al. 2009, in preparation). Our study is based on the complete (to envelope masses $\gtrsim 0.1 M_{\odot}$) sample of 39 Class 0 protostars in the Serpens, Perseus, and Ophiuchus molecular clouds, identified by Enoch et al. (2009) by comparing large-scale *Spitzer* IRAC and MIPS and Bolocam 1.1 mm continuum surveys of the three clouds.

⁷ We use definitions of Class 0, Class I, and Class II (André 1994) based on the bolometric temperature (Myers & Ladd 1993; Chen et al. 1995): $T_{\text{bol}} \leq 70$ K (Class 0); $70 \text{ K} < T_{\text{bol}} \leq 650$ K (Class I); $650 \text{ K} < T_{\text{bol}} \leq 2800$ K (Class II). We further assume that classes correspond to an evolutionary sequence (e.g., Robitaille et al. 2006): in Class 0, the protostar has accreted less than half its final mass ($M_* < M_{\text{env}}$), in Class I $M_* > M_{\text{env}}$, and in Class II the envelope has dispersed, leaving only a circumstellar disk.

⁵ *Spitzer* Fellow.

⁶ Jansky Fellow, NRAO.

Combining *Spitzer* Infrared Spectrograph (IRS) mid-infrared (MIR) spectra and high-resolution Combined Array for Research in Millimeter-wave Astronomy (CARMA) 230 GHz continuum imaging with radiative transfer modeling of this sample will help to address several fundamental questions about the structure and evolution of the youngest protostars: (1) how soon after the initial collapse of the parent core does a circumprotostellar disk form? (2) What fraction of the total circumprotostellar mass resides in the disk, and does this fraction vary with time? (3) Are large “holes” in the inner envelope, such as that found for IRAS 16293 by Jørgensen et al. (2005b), common at early times?

MIR spectra and millimeter maps provide complementary approaches to these questions. The amount of flux escaping at $\lambda \lesssim 50 \mu\text{m}$ from deeply embedded sources is very sensitive to the opacity close to the protostar, and thus the envelope structure (e.g., Jørgensen et al. 2005b). While the MIR flux is insensitive to disk properties, high-resolution millimeter continuum mapping can directly detect emission from dust grains in the disk. Millimeter observations with excellent uv -coverage, combined with radiative transfer models, can separate the disk from the envelope and constrain the disk mass and size.

Our ultimate goal is to characterize the disk mass, size, and inner envelope structure of typical low-mass Class 0 protostars, and to quantify any trends with evolutionary indicators. In this initial paper, we present results for Serpens FIRS 1, a well-known Class 0 source, which will serve as a test case for the full program.

2. SERPENS FIRS 1

FIRS 1 is located at $18^{\text{h}}29^{\text{m}}49^{\text{s}}.6 + 01^{\circ}15'21''.9$ (J2000)⁸ in the main core (Cluster A) of the Serpens Molecular Cloud. We adopt a distance of $d = 260 \pm 10$ pc (Straizys et al. 1996), and any quoted literature values are scaled to this distance. It is a well-known Class 0 protostar (e.g., Hurt & Barsony 1996) first noted in the far-infrared by Harvey et al. (1984), and also known by its submillimeter designation Serpens SMM 1 (Casali et al. 1993). There is a narrow $\lambda = 3.6$ cm bipolar radio jet at the position of FIRS 1 (Rodríguez et al. 1989; Curiel et al. 1993), indicating a powerful outflow that is also clearly seen in molecular lines (Davis et al. 1999; Curiel et al. 1996).

Figure 1 gives an overview of the FIRS 1 environment with *Spitzer* 24 μm and Bolocam 1.1 mm continuum maps of the Serpens main core. The nearest known YSO is approximately $25''$ away, or 6000 AU in projected distance (Harvey et al. 2007), and the nearest embedded protostar known to have an envelope is $45'' \approx 11,000$ AU away (Enoch et al. 2009).

FIRS 1 is referred to as Ser-emb 6 in Enoch et al. (2009), and is associated with the 1.1 mm Bolocam core Ser-Bolo 23 (Enoch et al. 2007). Based on Two Micron All Sky Survey (2MASS), *Spitzer*, and Bolocam data the bolometric luminosity is $11.0 L_{\odot}$,⁹ the bolometric temperature is 56 K, confirming the Class 0 designation, and the total envelope mass is $8.0 M_{\odot}$ (Enoch et al. 2009).

Previous high-resolution millimeter observations have placed limits on the mass of a compact disk in FIRS 1. Hogerheijde, van Dishoeck, & Salverda (1999) used observation from the Owens Valley Radio Observatory (OVRO) millimeter interferometer

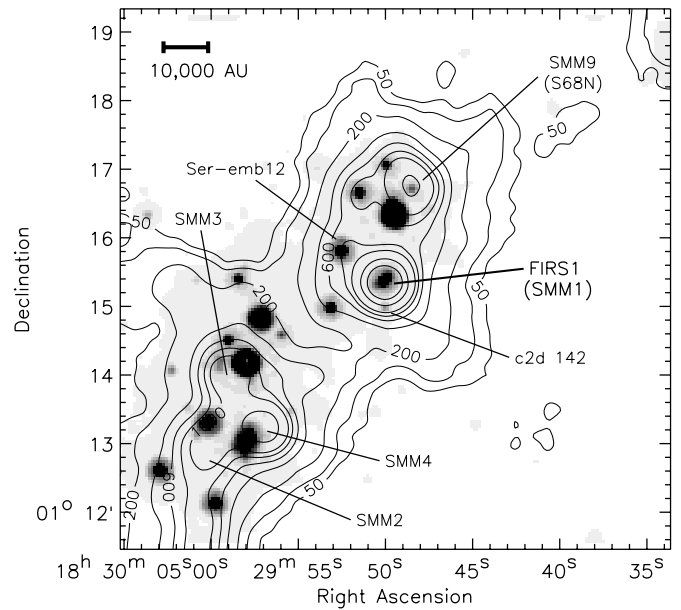


Figure 1. *Spitzer* 24 μm image of the immediate environment of Serpens FIRS 1, in the Serpens main core. Bolocam 1.1 mm continuum contours are overlaid. Submillimeter source designations for the brightest Casali et al. (1993) sources are indicated. The nearest embedded protostar to FIRS 1 is approximately $45''$ or 11,000 AU away (Ser-emb 12; Enoch et al. 2009), and the nearest YSO is $25''$ or 6000 AU away (c2d 142; Harvey et al. 2007).

to estimate a total mass (disk plus envelope) within 100 AU of $0.7 M_{\odot}$. Brown et al. (2000) place a lower limit on the disk mass of $\sim 0.1 M_{\odot}$ with submillimeter observations ($\nu \sim 350$ GHz) from the James Clerk Maxwell Telescope–Caltech Submillimeter Observatory (JCMT-CSO) single baseline interferometer.

3. OBSERVATIONS

3.1. *Spitzer* IRS Spectrum

Mid-infrared spectra were obtained with the IRS on the *Spitzer Space Telescope* (Werner et al. 2004; Houck et al. 2004) during 2007 October 5 with the Low Res 7.4–14.5 μm (SL1; $R \sim 100$), Hi Res 9.9–19.6 μm (SH; $R \sim 600$), and Hi Res 18.7–37.2 μm (LH; $R \sim 600$) modules. Integration times were 117 s in SL1, 189 s in SH, and 59 s in LH. Off-source or background spectra with the same integration times were also obtained for SH and LH.

Spectra were extracted from the *Spitzer* Science Center (SSC) pipeline version S16.1.0 BCD images using the reduction pipeline (Lahuis et al. 2006) developed for the “From Molecular Cores to Planet-forming Disks” *Spitzer* Legacy Program (“Cores to Disks” or c2d; Evans et al. 2003). We use the optimal point-spread function (PSF) extraction method of the pipeline, which is based on fitting the analytical cross dispersion point spread function, plus extended emission, interpolating over bad pixels. The one-dimensional spectra are flux calibrated using a spectral response function derived from a suite of calibrator stars, corrected for instrumental fringe residuals, and an empirical order matching algorithm is applied. PSF extraction was completed for both FIRS 1 and the background field; the final spectrum is the difference between them.

The resulting spectrum from 7.4 to 37.2 μm is shown in Figure 2. Each module is reduced separately, so the degree of agreement gives some idea of the reliability of calibration. Both the full reduced spectra (solid lines), and the average flux in wavelength bins of $\Delta\lambda \sim 0.75 \mu\text{m}$, $1.5 \mu\text{m}$, and $1 \mu\text{m}$ for SL1,

⁸ *Spitzer* position from Harvey et al. (2007).

⁹ Note that lower resolution HIRES IRAS fluxes (Hurt & Barsony 1996) and ISO-LWS spectra (Larsson et al. 2000) yield higher bolometric luminosities of $62 L_{\odot}$ and $95 L_{\odot}$, respectively, but these may be confused with nearby embedded protostars.

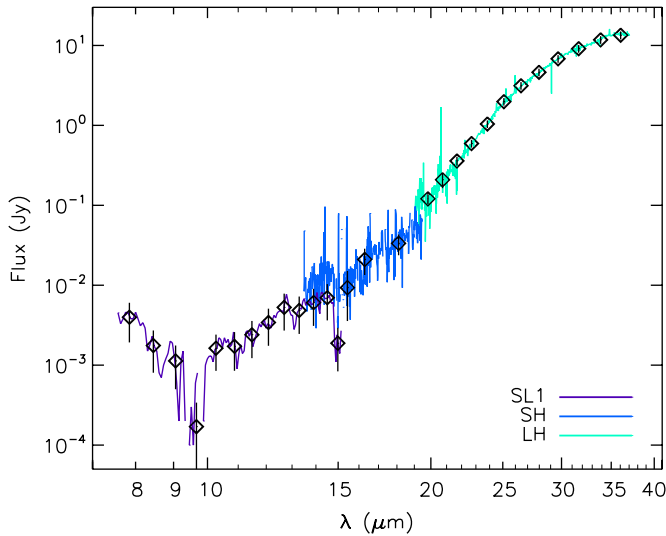


Figure 2. *Spitzer* IRS spectrum of Serpens FIRS 1, using the Low Res 7.4–14.5 μm (SL1), Hi Res 9.9–19.6 μm (SH), and Hi Res 18.7–37.2 μm (LH) modules. The low signal to noise SH data at $\lambda < 13.5 \mu\text{m}$ is not plotted. Binned data ($\Delta\lambda \sim 1 \mu\text{m}$) are overplotted as diamonds; error bars represent the error in the mean for each bin. Binned fluxes are used in the model fitting and given in Table 1.

(A color version of this figure is available in the online journal.)

SH, and LH, respectively, are shown. The SH spectrum has the lowest signal to noise, so it is binned on the coarsest grid. Only data with signal to noise greater than one (SL1, SH) or three (LH) are included in the binned points. Binned fluxes are listed in Table 1.

In Figure 2, the silicate absorption band at 9.7 μm is clearly visible, and a hint of the CO_2 ice band at 15 μm is also visible. A number of finer features in the LH spectrum are most likely real, but will not be discussed here.

3.2. CARMA 230 GHz Map

Continuum observations at $\nu = 230 \text{ GHz}$ ($\lambda = 1.3 \text{ mm}$) were completed with the CARMA, a 15 element interferometer consisting of nine 6.1 m and six 10.4 m antennas. Data were obtained in the B array (100–1000 m baselines), C array (30–350 m), D array (11–150 m), and E array (8–66 m) configurations between 2007 October 24 and 2008 December 31. These data were combined to provide uv -coverage from 4.5 to 500 $k\lambda$. Small seven-pointing mosaics were made in the compact configurations (D and E) in order to mitigate spatial filtering by the interferometer, and to more fully map the spatially extended protostellar envelope.

All three correlator bands were configured for continuum, 468 MHz bandwidth, observations. A bright quasar (1751+096) was observed approximately every 15 minutes to be used for complex gain calibration. Absolute flux calibration was accomplished using 5 minute observations of Uranus, Neptune, or MWC 349. The overall calibration uncertainty is approximately 20%, from the reproducibility of the phase calibrator flux on nearby days. A passband calibrator, typically 3C454.3, was observed for 15 minutes during each set of observations, and radio pointing was performed every two hours. Observations in the most extended B configuration utilized the Paired Antenna Calibration System (PACS) to correct for phase variations on minute timescales (see L. Pérez et al. 2009, in preparation).

Calibration and imaging were accomplished with the MIRIAD data reduction package (Sault et al. 1995). The re-

Table 1
Spitzer IRS and Broadband *Spitzer*, SHARC-II, and Bolocam Fluxes Used in the SED Fits

Wavelength (μm)	Flux (Jy)	Uncertainty (Jy)	Aperture (arcsec)	Instrument
3.6	0.00085	0.00016	2.2	IRAC
4.5	0.0026	0.0005	2.2	IRAC
5.8	0.0023	0.0005	2.2	IRAC
7.8	0.004	0.002	3.7	IRS (SL1)
8.5	0.0018	0.0010	3.7	IRS (SL1)
9.1	0.0011	0.0006	3.7	IRS (SL1)
9.7	0.0002	0.0003	3.7	IRS (SL1)
10.3	0.0016	0.0008	3.7	IRS (SL1)
10.9	0.0017	0.0009	3.7	IRS (SL1)
11.5	0.0024	0.0012	3.7	IRS (SL1)
12.1	0.0034	0.0017	3.7	IRS (SL1)
12.7	0.005	0.003	3.7	IRS (SL1)
13.3	0.005	0.002	3.7	IRS (SL1)
13.9	0.006	0.003	3.7	IRS (SL1)
14.5	0.007	0.003	3.7	IRS (SL1)
15.0	0.0019	0.0011	3.7	IRS (SL1)
15.4	0.009	0.006	10.5	IRS (SH)
16.3	0.021	0.008	10.5	IRS (SH)
18.1	0.033	0.010	10.5	IRS (SH)
19.8	0.121	0.017	11.1	IRS (LH)
20.7	0.21	0.04	11.1	IRS (LH)
21.7	0.36	0.04	11.1	IRS (LH)
22.7	0.59	0.07	11.1	IRS (LH)
23.8	1.04	0.11	11.1	IRS (LH)
25.1	2.0	0.2	11.1	IRS (LH)
26.5	3.1	0.3	11.1	IRS (LH)
28.0	4.6	0.5	11.1	IRS (LH)
29.7	6.8	0.7	11.1	IRS (LH)
31.6	9.1	1.0	11.1	IRS (LH)
33.9	11.8	1.3	11.1	IRS (LH)
36.0	13.4	1.5	11.1	IRS (LH)
70	77	41	17	MIPS
350	195	79	40	SHARC II
1100	5.9	1.2	40	Bolocam

Notes. Apertures in which fluxes are calculated correspond to the instrument PSF, with the exception of the SHARC-II and Bolocam fluxes. Calibrated IRS fluxes are averaged in wavelength bins of $\Delta\lambda \sim 0.75 \mu\text{m}$, $1 \mu\text{m}$, and $1.5 \mu\text{m}$ for SL1, SH, and LH, respectively, as described in Section 3.1. The IRS flux is the mean within a bin, and the instrumental uncertainty is the error in the mean (σ/\sqrt{N}). All uncertainties include a 10% systematic uncertainty in addition to the instrumental uncertainty.

sulting 230 GHz map of FIRS 1 is shown in Figure 3, with maps made at three resolutions: short baseline data only (D and E configurations), all data, and long baseline data only (B and C configurations). The direction of the 3.6 cm jet (Rodríguez et al. 1989; Curiel et al. 1993) is shown for reference.

The map including all data was inverted with natural weighting, cleaned with a Steer CLEAN algorithm (Steer et al. 1984), and restored with an $0''.94 \times 0''.89$ beam. The rms noise level in the central region is $6.7 \text{ mJy beam}^{-1}$, the peak and total flux from a Gaussian fit are $0.42 \text{ Jy beam}^{-1}$ and 1.38 Jy (P.A. = -4 deg), and the deconvolved FWHM size is $1''.6 \times 1''.2$. The synthesized beam corresponds to approximately 240 AU, while the longest baselines provide a resolution better than 100 AU ($0''.46 \times 0''.40$). A Gaussian fit to the long baseline data yields P.A. = 25 deg , approximately 75 deg from the 3.6 cm jet axis (P.A. = -50 deg).

The extended, complex nature of the source is apparent, thanks to the excellent uv -coverage achieved with multiple

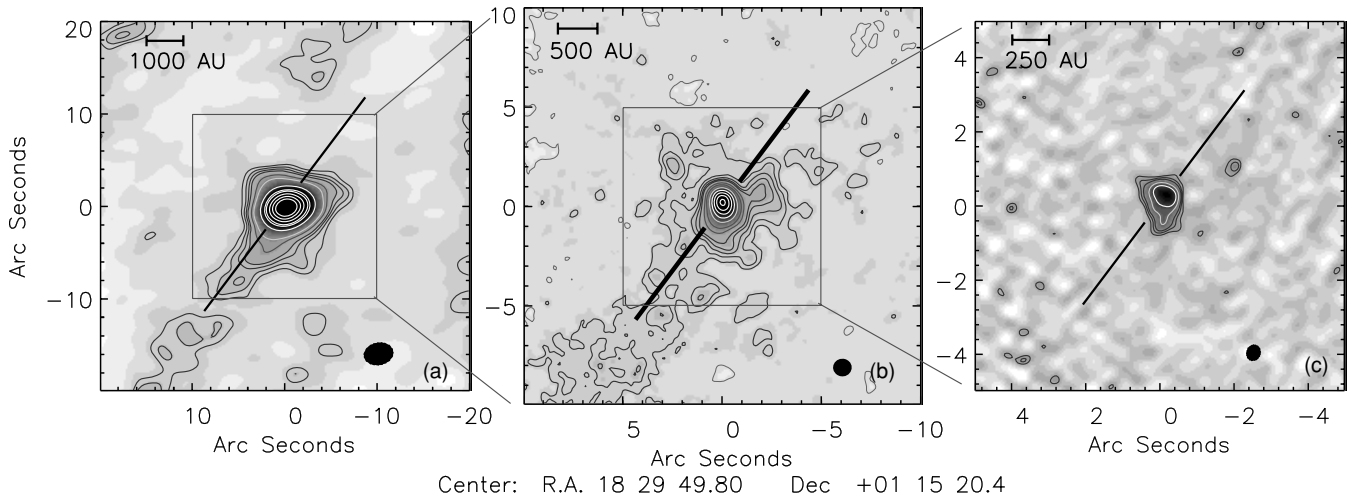


Figure 3. CARMA 230 GHz maps of Serpens FIRS 1 for short baseline data only (D,E configurations; panel (a)), all data (panel (b)), and long baseline data only (B, C configurations; panel (c)). Contours in panel (b) are (2,4...10,15,20,30...70) times the 1σ rms of $6.7 \text{ mJy beam}^{-1}$, for a synthesized beam of $0''.94 \times 0''.89$ (shown, lower right). Contours in panels (a) and (c) are similar but start at 4σ and 6σ , respectively, and panel A has additional contours at $(90\sigma, 110\sigma, 130\sigma)$. Note the change in scale in each panel. The direction of the 3.6 cm jet (Rodríguez et al. 1989; Curiel et al. 1993) is shown for reference.

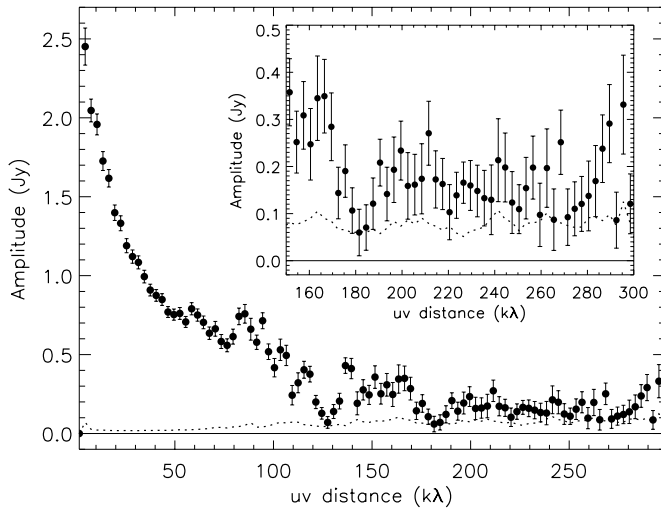


Figure 4. CARMA 230 GHz visibility amplitude versus uv -distance for Serpens FIRS 1. Observations in the B, C, D, and E CARMA antenna configurations provide uv -coverage from approximately $4.5 k\lambda$ to $500 k\lambda$. The expected value in the case of zero signal, or amplitude bias, is indicated by a dotted line and is typically small (less than 0.1 Jy).

configurations. Although it is difficult to see the more extended envelope even in the short baseline map, it is clearly visible as an amplitude peak at uv -distances $< 20 k\lambda$ in a plot of amplitude versus uv -distance (Figure 4). Note that the interferometer does filter out flux at uv -distances less than $4 k\lambda$, corresponding to the separation of the closest antenna pairs. Figure 4 shows that most of the source flux is concentrated at low and intermediate uv -distances (extended structure), but the source is clearly detected at uv -distances greater than $200 k\lambda$, indicating an unresolved or marginally resolved compact ($< 1''$) component. Values of the 230 GHz flux as a function of uv -distance are given in Table 2.

3.3. Spitzer, Bolocam, and SHARC-II Broadband Data

Broadband infrared data for FIRS 1 are taken from the “Cores to Disks” *Spitzer* Legacy program (Evans et al. 2003), which imaged approximately 1 deg^2 in the cloud with IRAC and MIPS

Table 2
CARMA 230 GHz Visibilities

uv -distance ($k\lambda$)	Flux (Jy)	Uncertainty (Jy)
4.50	2.45	0.12
7.50	2.05	0.07
10.5	1.96	0.07
13.5	1.70	0.06
16.5	1.60	0.06
19.5	1.38	0.05
22.5	1.31	0.05
25.5	1.17	0.04
28.5	1.10	0.04
31.5	1.07	0.04

Notes. Visibilities and uncertainties used in the model fits. The amplitude bias, or expected value for zero signal, has been subtracted from the data.

(This table is available in its entirety in a machine-readable form in the online journal. A portion is shown here for guidance regarding its form and content.)

(Harvey et al. 2006, 2007). The same region was mapped at $\lambda = 1.1 \text{ mm}$ with the Bolocam bolometer array (Glenn et al. 2003) at the Caltech Submillimeter Observatory (CSO; Enoch et al. 2007). These data provide wavelength coverage from $\lambda = 3.6$ to $1100 \mu\text{m}$ (IRAC 3.6, 4.5, 5.8, $8.0 \mu\text{m}$; MIPS 24, 70, $160 \mu\text{m}$; Bolocam $1100 \mu\text{m}$). FIRS 1 is not detected in the 2MASS catalogs.

Broadband fluxes are used to determine the bolometric luminosity and temperature ($11.0 L_{\odot}$ and 56 K), and are included in the model fits in Section 5, below. The total envelope mass ($8.0 M_{\odot}$) is calculated from the total flux in a $40''$ aperture at $\lambda = 1.1 \text{ mm}$, assuming the envelope is optically thin at 1.1 mm , a dust opacity of $\kappa_{1 \text{ mm}} = 0.0114 \text{ cm}^2 \text{ g}^{-1}$ (Ossenkopf & Henning 1994), and a dust temperature of $T_D = 15 \text{ K}$ (see Enoch et al. 2009 for more details).

We also include in the observed spectral energy distribution (SED) the $350 \mu\text{m}$ continuum flux (M. Dunham et al. 2009, in preparation), obtained with SHARC-II (Dowell et al. 2003)

at the CSO. The SHARC-II flux samples the peak of the SED, and helps constrain the long-wavelength side of the model SED. All fluxes used in the SED fit are given in Table 1, including uncertainties, aperture diameters, and instrument used for the observations.

4. RADIATIVE TRANSFER MODEL

To model the observed emission from FIRS 1, we use the two-dimensional Monte Carlo radiative transfer code RADMC of Dullemond & Dominik (2004). RADMC performs both Monte Carlo radiative transfer to derive the temperature distribution from an input density distribution, and ray tracing to produce images and photometry in specified apertures. We adopt a density profile very similar to that of Crapsi et al. (2008), which includes three components: the envelope, the outflow cavity, and the disk. For both the envelope and disk, we use the dust opacities from Table 1, Column 5 of Ossenkopf & Henning (1994) for dust grains with thin ice mantles, including scattering, interpolated onto the necessary wavelength grid. We note that although this is a young source, there could be significant difference in the dust properties of the disk and envelope, as have been demonstrated in some Class I sources (Wolf et al. 2003).

The envelope density profile is that of a rotating, collapsing sphere (Ulrich et al. 1967),

$$\rho_{\text{env}}(r, \theta) = \rho_0 \left(\frac{r}{R_c} \right)^{-1.5} \left(1 + \frac{\mu}{\mu_0} \right)^{-0.5} \left(\frac{\mu}{\mu_0} + 2\mu_0^2 \frac{R_c}{r} \right)^{-1}, \quad (1)$$

where $\mu = \cos \theta$, $R_c = R_{\text{cent}}$ is the centrifugal radius, and ρ_0 is the density at $(r, \theta) = (R_c, 0)$, which is set by the total envelope mass $M_{\text{env}} = 8 M_{\odot}$. A gas-to-dust mass ratio of 100 and mean molecular weight of 2.33 are included. Here, $\mu_0 = \cos \theta_0$ is the solution of the parabolic motion of an infalling particle, given by

$$\left(\frac{r}{R_{\text{cent}}} \right) \left(\frac{\mu_0 - \mu}{\mu_0 \sin^2 \mu_0} \right) = 1. \quad (2)$$

The model has no time dependence; R_{cent} is not a true centrifugal radius defined by the conservation of angular momentum during collapse, but simply a set radius where the density peaks, and inward of which the density drops to very low values. The envelope outer radius R_{out} is the maximum value of the radial grid, so the envelope density is zero for $r > R_{\text{out}}$. The outflow cavity is defined by setting the density to zero in the region where $\cos \theta_0 > \cos(\text{Ang}/2)$. This results in a funnel-shaped cavity, which is conical only at large scales where Ang is the full opening angle.

The disk density is given by a power-law dependence in radius and a Gaussian dependence in height:

$$\rho_{\text{disk}}(r, \theta) = \frac{\Sigma_0}{\sqrt{2\pi} H(r)} \left(\frac{r}{R_{\text{disk}}} \right)^{p1} \exp \left[-\frac{1}{2} \left(\frac{r\mu}{H(r)} \right)^2 \right], \quad (3)$$

where Σ_0 is set by the input disk mass M_{disk} . At R_{disk} , $p1$ changes from -1 to -12 , effectively setting the disk radius. The scale-height variation (flaring) is given by $H(r) = r(H_0/R_{\text{disk}})(r/R_{\text{disk}})^{p2}$. We set $p2 = 2/7$, corresponding to the self-irradiated passive disk of Chiang & Goldreich (1997). Given that the disk is in large part hidden by the envelope, a much simpler description would likely work just as well, but we choose to follow the setup of Crapsi et al. (2008) here. Most of the disk parameters are held fixed for the main model grid, with only M_{disk} and R_{disk} varying.

Table 3 lists the range of input values for the model input parameters, some of which are held fixed. The internal luminosity is set by the bolometric luminosity; it is input to the model as the stellar luminosity, although most likely a majority of the luminosity is due to accretion. We do not include an interstellar radiation field here, as the luminosity of any reasonable field is negligible compared to the internal luminosity of FIRS 1, and has only a negligible effect on the long-wavelength SED.

Small single parameter grids were run to test that “fixed” parameters have no significant affect on the model SED or millimeter visibilities. The scale height (H_0) and flaring ($p1$) of the disk do affect the 3–20 μm fluxes, although only for Incl < 10 deg, where there is too much NIR flux to match the data regardless of the value of these parameters. A very puffy disk ($H_0 \gtrsim 0.5 R_{\text{disk}}$) produces more emission in this range, while a very thin disk ($H_0 \lesssim 0.1 R_{\text{disk}}$) produces less emission. Similarly, a flared disk produces more MIR emission than one with no flaring.

5. RESULTS

To determine the best-fit envelope parameters we run a grid of models varying R_{out} , R_{cent} , Ang, and Incl. This results in a total of 588 envelope models, each observed at 13 inclination angles. A nominal disk of $M_{\text{disk}} = 0.01 M_{\odot}$, $R_{\text{disk}} = 150$ AU is used for all envelope models. A separate grid varying M_{disk} and R_{disk} with fixed envelope parameters includes 140 models. Our tests show that the disk has little effect on the SED for this source, making separate grids feasible.

The model grids are compared to the SED and 230 GHz visibilities with an χ^2 analysis using data from Tables 1 and 2. Contour plots of the resulting reduced χ^2 ($\tilde{\chi}^2$) are shown in Figure 5, where contours for both the SED and 230 GHz visibilities are plotted. The model and data visibilities are calculated by the same method, using vector averaging in radial annuli.

The best-fitting model ($R_{\text{out}} = 5000$ AU, $R_{\text{cent}} = 600$ AU, Ang = 20 deg, Incl = 15 deg, $M_{\text{disk}} = 1.0 M_{\odot}$, $R_{\text{disk}} = 300$ AU) is compared to the data in Figure 6. The same envelope model with no disk is also shown for reference, as is an envelope model with no inner envelope hole ($R_{\text{cent}} = 20$ AU; dotted line). Determination of the best-fit model from Figure 5 is described in Sections 5.1 and 5.2. Due to the small uncertainties and the limited number of models, the reduced χ^2 values for even the best-fit model are still fairly high ($\tilde{\chi}^2 \sim 13$ and 5 for the SED and visibilities, respectively). The bolometric temperature and luminosity of the best-fit model are 35.3 K and $17.3 L_{\odot}$. The bolometric luminosity differs from the input stellar luminosity due to inclination effects.

While we only show the best-fit model here, there is a range of values for each parameter that can reasonably fit the data, as determined by eye from χ^2 plots and visual inspection of the SED fits. We find that the envelope parameters have the following reasonable ranges: $R_{\text{out}} \sim 5000$ – 7000 AU, $R_{\text{cent}} \sim 400$ – 600 AU, Ang ~ 10 – 30 deg, and Incl ~ 10 – 25 deg. Reasonable disk parameters are $M_{\text{disk}} \sim 0.7$ – $1.5 M_{\odot}$, and $R_{\text{disk}} \sim 200$ – 500 AU.

Literature fluxes are shown in comparison to our data and the best-fit model SED in Figure 7. Shown are IRAS HIRES 25, 60, and 100 μm from Hurt & Barsony (1996), SCUBA 450 and 850 μm peak fluxes from Davis et al. (1999), JCMT 800, 1100, 1300, and 2000 μm fluxes from Casali et al. (1993), and the OVRO 3 mm flux from Testi & Sargent (1998). They

Table 3
Range of Parameter Values Used in the Radiative Transfer Model Grid

Parameter	Fixed?	Range	Description
Protostar			
L_{star}	Y	$11 L_{\odot}$	Internal luminosity
T_{star}	Y	4000 K	Protostar effective temperature
Envelope and Outflow			
M_{env}	Y	$8.0 M_{\odot}$	Total mass of envelope
R_{out}	N	3000–12000 AU	Outer radius of envelope
R_{cent}	N	50–1000 AU	Centrifugal (inner) radius of envelope
Ang	N	5–80 deg	Outflow opening angle
Incl	N	5–90 deg	Inclination angle
Disk			
M_{disk}	N	$0.0\text{--}3.0 M_{\odot}$	Disk mass
R_{disk}	N	50–1000 AU	Disk radius
H_0	Y	$0.2 R_{\text{disk}}$	Disk vertical pressure scale height
p_1	Y	–1.0	Disk surface density radial power law ($r < R_{\text{disk}}$)
p_2	Y	2/7	Power law for H(R) (disk flaring)

Notes. The internal luminosity is set by the bolometric luminosity of the source, determined from the broadband SED, and the envelope mass is set by the 1.1 mm Bolocam single dish flux (see Enoch et al. 2009). Ang is the full outflow opening angle. Incl is the line-of-sight inclination angle of the disk: 0 deg is face-on, 90 deg is edge-on. Stellar, envelope, and disk parameters are discussed in Section 4.

cannot be compared directly to the model SED because many of them are peak fluxes calculated in small apertures; circles show the corresponding model values computed in similar apertures. While there is not perfect agreement, the model is roughly consistent with the literature values, with the exception of IRAS fluxes. The IRAS observations are lower resolution than the *Spitzer* maps, and FIRS 1 may be confused with nearby protostars (24''–45'' away). Literature fluxes are not included in the $\tilde{\chi}^2$ fitting.

5.1. Envelope Structure

Envelope parameters are determined first, using the grid of envelope models (Figures 5(a)–(c)). The four-dimensional $\tilde{\chi}^2$ space is collapsed along the parameters not plotted in each panel. We conclude below that $R_{\text{out}} \leq 7000$ AU based on the 230 GHz visibility $\tilde{\chi}^2$ contours in panel (a), so only models with $R_{\text{out}} \leq 7000$ AU are included in panels (b) and (c) to avoid complicating the plots (because many models with $R_{\text{out}} > 7000$ AU can fit the SED).

With a few exceptions, the SED is much more sensitive to envelope parameters than are the 230 GHz visibilities. R_{out} , however, is only mildly constrained by the SED and is somewhat degenerate with R_{cent} . Increasing either parameter lowers the total opacity of the envelope, allowing more MIR emission to escape. In addition, for $R_{\text{out}} > 7000$ AU, the SED provides no constraint on R_{cent} because the opacity through the envelope is already quite low. In this case, the 230 GHz data do help constrain the envelope parameters because visibility amplitudes at uv -distance $\lesssim 30 k\lambda$ trace extended emission. A narrow peak in the uv plane (Figure 4) corresponds to a large envelope outer radius, and a wider peak to a small outer radius. The best compromise between the visibilities preferring smaller R_{out} and the SED preferring larger R_{out} is $R_{\text{out}} \sim 5000$ AU (Figure 5(A)). The value of R_{cent} with the lowest SED $\tilde{\chi}^2$ in this case is 600 AU.

A more compact envelope creates a high opacity to shorter wavelength emission, thus a larger R_{cent} is needed to decrease

opacity close to the protostar and to match the observed NIR and MIR emission. For $R_{\text{out}} \leq 7000$ AU, the range of reasonable centrifugal radii are $R_{\text{cent}} = 400\text{--}700$ AU. There are a few models with small R_{cent} and low $\tilde{\chi}^2$; when the viewing angle is just down the edge of the outflow (Incl = Ang/2) in a dense envelope ($R_{\text{out}} = 4000$ AU). In these special cases, the opacity is lowered just enough to give a similar emergent SED as models with a large inner envelope hole.

A compact envelope with $R_{\text{out}} \sim 5000$ AU is consistent with the crowded star formation region in which FIRS 1 is located. The nearest embedded protostar that is known to have an envelope is 45'', or approximately 11,000 AU away, and several other embedded sources are within a few arcminutes (Enoch et al. 2009). While we do not know the actual three-dimensional distances, envelopes with radii $R_{\text{out}} \sim 5000$ AU are certainly reasonable in this clustered region.

Both the outflow opening angle and inclination are fairly narrowly constrained by the SED (Figures 5(b) and (c)). There is a degeneracy between Ang and Incl; all models where the line of sight is directly within the outflow cavity (Incl < Ang/2) have very high $\tilde{\chi}^2$ values because they produce a large excess of NIR emission. The SED is best fit by models with low inclinations (Incl < 35 deg); larger inclinations produce very high extinction in the MIR and cannot match the observed MIR flux. Low inclinations may be in conflict with the orientation of the 3.6 cm jet, which has been interpreted as being almost in the plane of the sky based on proper motion of emission knots in the jet (Moscadelli et al. 2006).

To summarize, the short uv -spacing visibility data favor small outer radii, while the SED favors larger outer radii, with the best compromise lying at $R_{\text{out}} \sim 5000$ AU. For $R_{\text{out}} = 5000$ AU, the SED $\tilde{\chi}^2$ is minimized for $R_{\text{cent}} = 600$ AU (panel (a) of Figure 5). With R_{cent} set to 600 AU, it is straightforward to determine the best-fit Ang and Incl from the SED χ^2 curves in panels (b) and (c).

None of the models accurately reproduce the shape of the silicate absorption feature or the slope of the spectrum from 10 to 20 μm , although the uncertainties on the observed fluxes

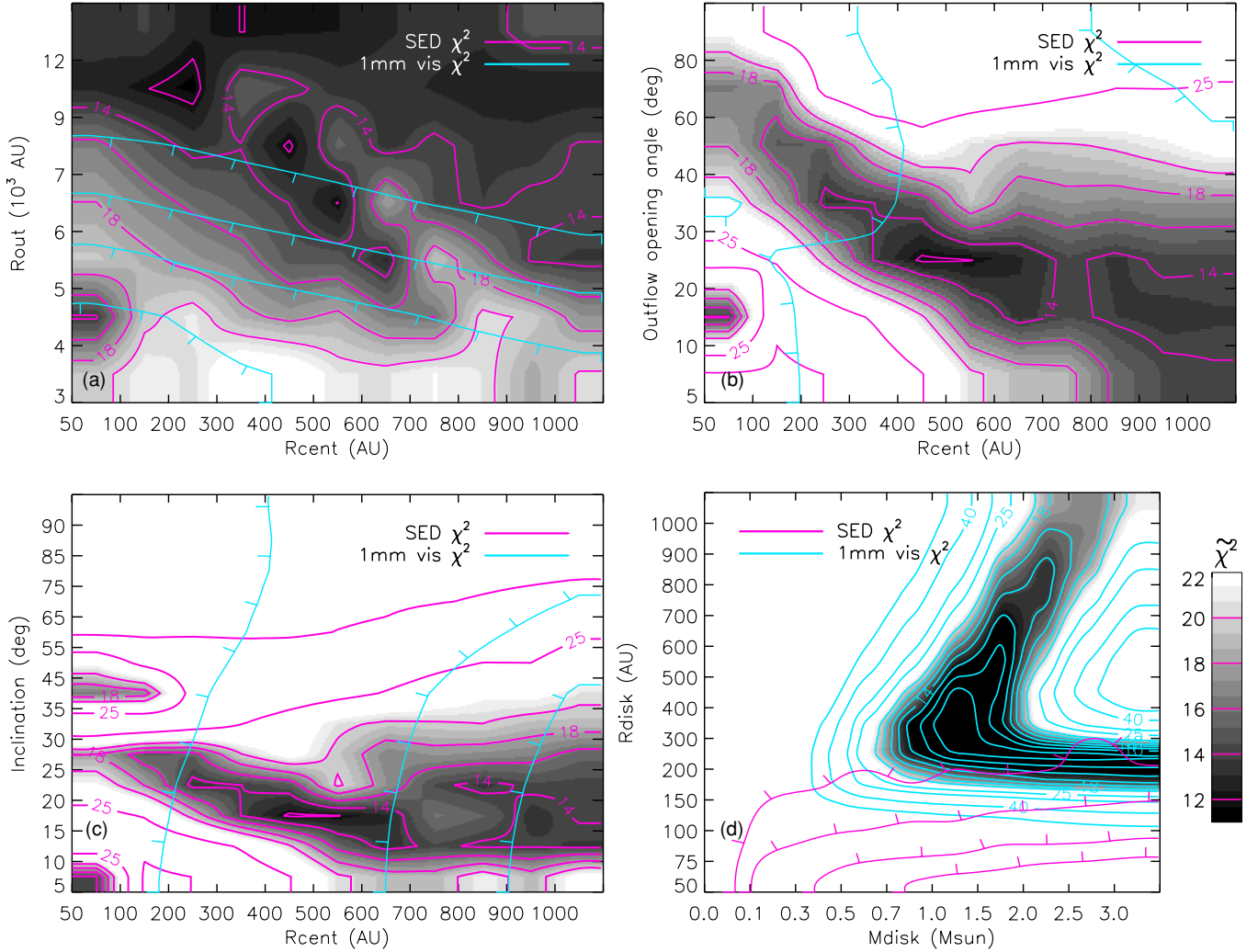


Figure 5. Reduced χ^2 contours resulting from fitting the observed SED and CARMA 230 GHz visibilities (Tables 1 and 2) to the grid of envelope and disk models. Models have been run for the full parameter ranges shown; the model grid resolution corresponds to the axis labels (e.g., R_{cent} values of 50, 100, 200, 300... 1000 AU), but the χ^2 distribution has been smoothed for a better visual representation. Contours from fits to the both the SED (magenta) and visibilities (cyan, tick marks indicate downhill direction) are shown, although envelope parameters (panels (a)–(c)) are primarily constrained by the SED, while disk parameters (panel (d)) are constrained by the millimeter visibilities. In panels (a)–(c) the χ^2 distribution is collapsed along the parameters not plotted. The lowest contour plotted is $\chi^2 = 8$. (A color version of this figure is available in the online journal.)

are also quite high in this region. This is most likely a feature of the dust model and not the envelope density profile. Similarly, the dust model does not include the $15 \mu\text{m}$ CO_2 ice absorption feature.

Note that the input stellar luminosity ($11 L_{\odot}$) is based on the bolometric luminosity calculated before the SHARC-II $350 \mu\text{m}$ was available, and thus is lower than the bolometric luminosity of the best-fitting model ($18 L_{\odot}$). Increasing the stellar luminosity to $18 L_{\odot}$ does not change the results dramatically; the best-fit centrifugal radius is a bit lower, 400 AU, without changing the other parameters. The reasonable range of R_{cent} is much larger however, allowing for R_{cent} as low as 50 AU for larger outflow opening angles (e.g., 40 deg).

5.2. Disk Structure

After the envelope parameters (R_{cent} , R_{out} , Ang, Incl) have been determined, we run a separate grid in disk mass and radius with envelope parameters fixed. The resulting χ^2 contours are shown in Figure 5(d). Disk parameters are entirely constrained

by the CARMA 230 GHz visibilities; the SED is insensitive to both M_{disk} and R_{disk} . A quite massive ($M_{\text{disk}} \sim 0.7\text{--}1.5 M_{\odot}$) and resolved ($R_{\text{disk}} \sim 200\text{--}500$ AU, compared to the maximum resolution of 100 AU) disk is required to account for the significant flux at intermediate uv -distances (20–100 $k\lambda$; Figure 6).

Typically, only a lower limit can be placed on the disk mass because once the disk emission becomes optically thick larger masses do not increase the millimeter flux. Here, however, because the disk is resolved the mass is more tightly constrained. For FIRS 1, fitting the visibilities out to maximum uv -distances from 50 to 300 $k\lambda$ produces the same best-fit disk parameters, although the goodness of fit increases with more data. The uv -coverage required to get a good fit should depend on the disk and envelope structure.

Disk properties derived by fitting the 230 GHz visibilities are relatively insensitive to the assumed envelope parameters. It is true that a somewhat less massive disk would be required if there were no inner envelope hole; for example for $R_{\text{cent}} = 50$ AU, the best fit is for $M_{\text{disk}} \sim 0.4$, $R_{\text{disk}} \sim 400$ AU. However, for envelope parameters with any reasonable fit to the SED (for example, $R_{\text{cent}} = 400$ AU, $R_{\text{out}} = 7000$ AU), $M_{\text{disk}} = 1.0 M_{\odot}$

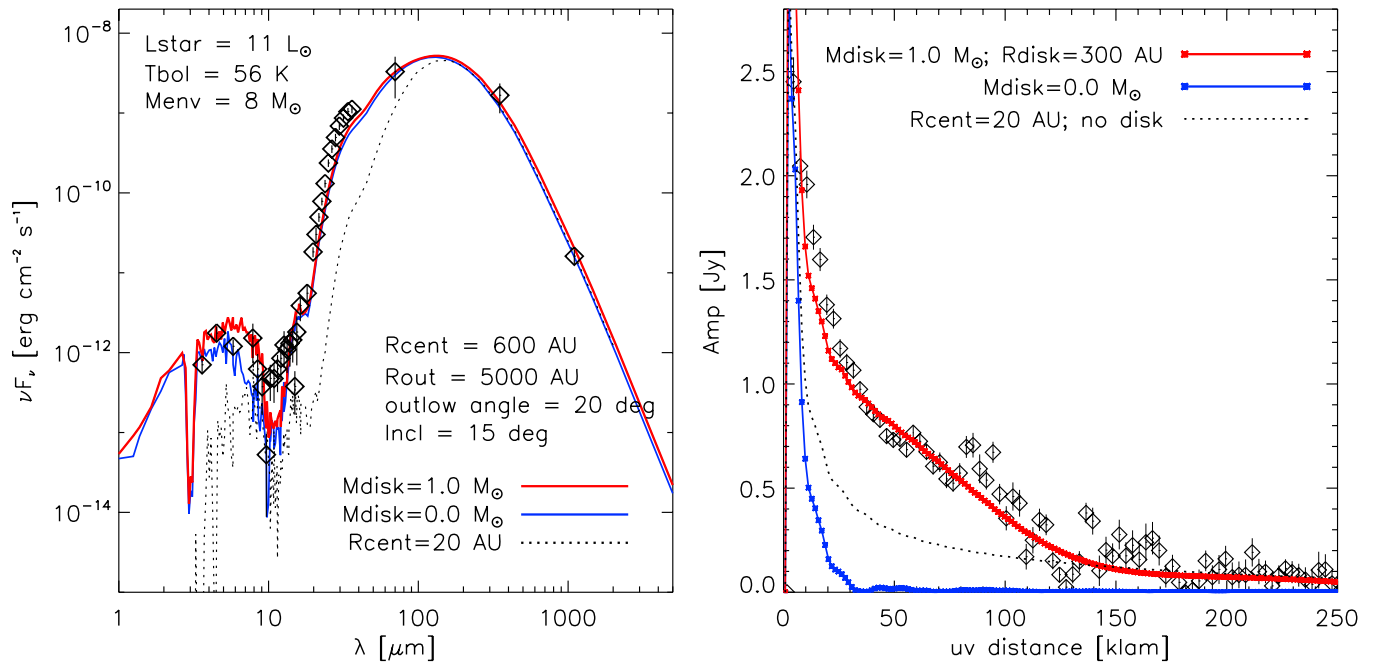


Figure 6. Best-fit envelope and disk model, compared to the observed SED (left) and 230 GHz visibilities (right). The SED includes the binned IRS spectra and broadband data from 3.6–1100 μ m (Table 1). Three models are shown for comparison: the best-fit envelope and disk (red), the best fit envelope with no disk (blue), and a model with no inner envelope hole ($R_{\text{cent}} = 20$ AU; dotted). The envelope-only model ($M_{\text{disk}} = 0 M_\odot$) indicates the relative contributions of the envelope and disk to the 230 GHz visibility amplitudes.

(A color version of this figure is available in the online journal.)

and $R_{\text{disk}} = 300$ AU remain the best fit to the 230 GHz visibilities.

The disk mass is also reasonably robust to uncertainties in the envelope mass ($8 M_\odot$) and 230 GHz calibration. For $M_{\text{env}} = 10 M_\odot$ the best-fit disk is unchanged, because only the amplitude of the narrow peak at small uv -distances is affected by the envelope mass. For $M_{\text{env}} = 6 M_\odot$, a slightly larger, more massive disk ($M_{\text{disk}} \sim 1.5 M_\odot$, $R_{\text{disk}} \sim 400$ AU) is required to account for the decrease in envelope flux at small uv -distances. The overall fit is poorer than for $M_{\text{env}} = 8 M_\odot$, however. Systematic uncertainties in the CARMA 230 GHz fluxes have a slightly larger effect, with a 30% change in overall flux calibration producing a corresponding 30% change in the disk mass: $M_{\text{disk}} \sim 0.5$ – $0.7 M_\odot$ for a 30% decrease, and $M_{\text{disk}} \sim 1.5$ – $2.0 M_\odot$ for a 30% increase.

5.3. Other Models

Here, we compare our models to other disk and envelope models. This serves both as a check on our derived envelope and disk parameters by indicating which conclusions are dependent on the density model, and a test that our models give the most reasonable fit to the data.

Hogerheijde et al. (1999) observed FIRS 1 with the OVRO interferometer at 3.4, 2.7, and 1.4 mm. They used a power-law envelope model plus a point source, with the dust temperature envelope model set at -0.4 and fixed inner and outer envelope radii of 100 and 8000 AU. These millimeter data were best fit by an envelope with mass $6 M_\odot$ and density power law -2.0 , plus an unresolved point source of approximately $0.7 M_\odot$. Hogerheijde et al. (1999) note that they are unable to separate the inner envelope from any disk emission, and thus cannot place a meaningful limit on the disk itself. Compared to the Hogerheijde et al. (1999) uv -coverage, 10–180 $k\lambda$ at 1.4 mm, our CARMA observations trace much more of the envelope (down to 4.5 $k\lambda$), allowing us to separately model

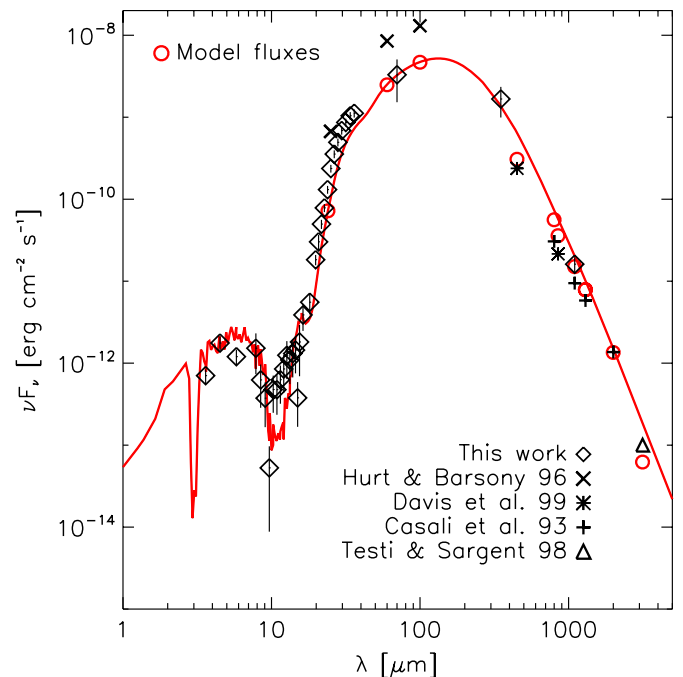


Figure 7. Best-fit model compared with literature fluxes: IRAS HIREs 25, 60, 100 μ m (Hurt & Barsony 1996), SCUBA 450, 850 μ m (peak fluxes; Davis et al. 1999), JCMT 800, 1100, 1300, 2000 μ m (Casali et al. 1993), and OVRO 3 mm (Testi & Sargent 1998). The model has been computed in apertures consistent with the literature measurements (circles). IRAS fluxes are based on lower resolution data than the *Spitzer* fluxes used here, and may be confused with nearby protostars. Literature fluxes are not used in the SED fit.

(A color version of this figure is available in the online journal.)

and remove the envelope contribution. Our data also have much higher signal to noise on long baselines (uv -distances $> 100 k\lambda$).

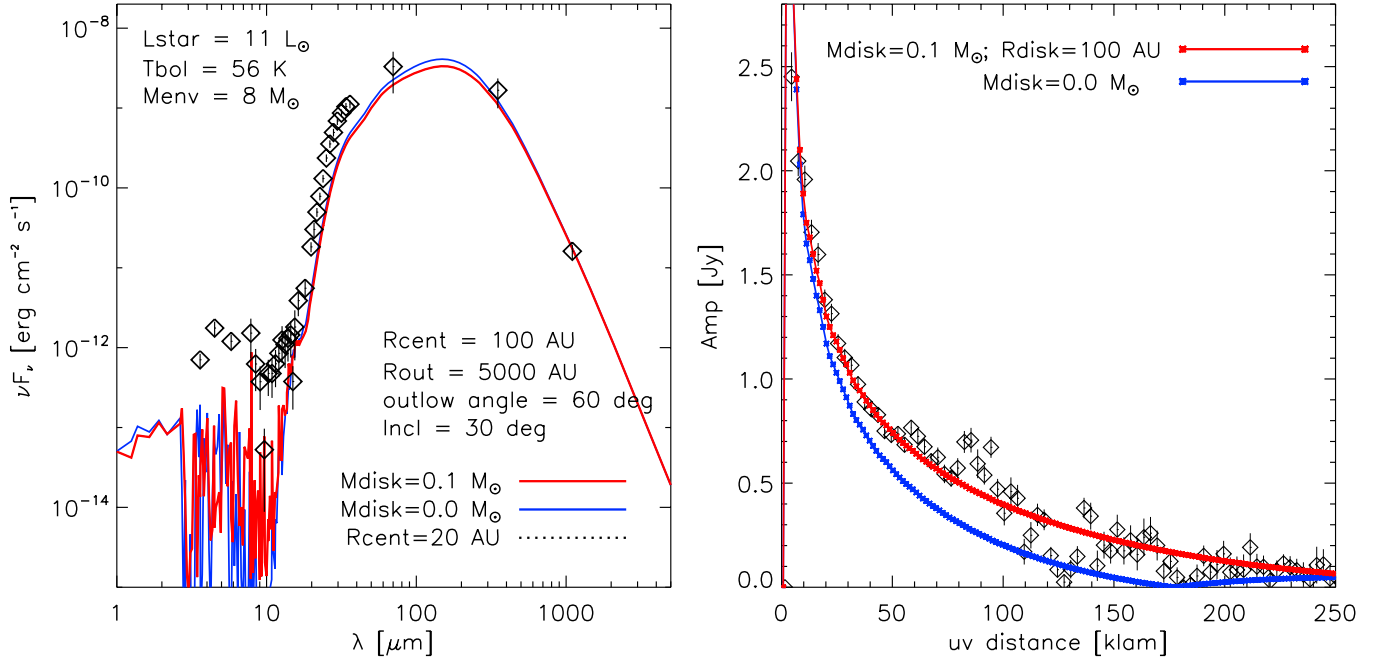


Figure 8. Best-fit power law envelope model, $\rho \propto r^{-2}$, compared to the observed SED and 230 GHz visibilities. A steep power law alleviates the need for a massive disk ($M_{\text{disk}} = 0.1 M_{\odot}$, $R_{\text{disk}} = 100$ AU is the best fit), but the power-law models are unable to match the observed MIR *Spitzer* fluxes.

(A color version of this figure is available in the online journal.)

In addition to the rotating, collapsing spheroid (or “Ulrich”) envelope models described in Section 4, we also ran a small grid of models with a simple power-law envelope density profile ($\rho \propto r^{-p}$), plus a conical cavity. A steep power law, $\rho \propto r^{-2}$, provides a reasonable fit to the visibilities without requiring a massive disk or large inner envelope hole. The best fit is for $M_{\text{disk}} = 0.1 M_{\odot}$, $R_{\text{disk}} = 100$ AU, and $R_{\text{cent}} = 100$ AU, as shown in Figure 8. Here, the emission at intermediate uv -distances is filled in by the envelope, which reaches high densities close to the protostar, thus requiring less disk emission. But, only a special combination of outflow opening angle and inclination can come close to matching the SED (Ang = 40 deg, Incl = 25 deg, or Ang = 60 deg, Incl = 30 deg; looking down the edge of a wide outflow cavity), and even the best-fit model gives a much poorer fit to the SED than the Ulrich models. In general, the power-law models seem unable to reasonably fit the NIR and MIR emission, although only $p = -2$ and -1.5 have been tested here.

The ability of the power-law envelope model to fit the visibilities without a large disk is consistent with some previous studies that have found that disks are often not required to millimeter data of Class 0 and Class I sources (e.g., Looney et al. 2000). The results here demonstrate that it is necessary to include both spectral and visibility data in order to fit a consistent disk and envelope model.

We use the online SED fitting tool of Robitaille et al. (2007) as another estimate of the envelope parameters, although the 230 GHz visibilities cannot be included in the fit. Robitaille et al. (2007) use an envelope setup similar to ours, with the envelope infall rate \dot{M}_{env} setting the fiducial density ρ_0 (rather than M_{env} as used here). The best-fit model corresponds to a protostar with age $t = 2 \times 10^5$ yr, $M_* = 1.8 M_{\odot}$, $R_* = 7 R_{\odot}$, $T_* = 4400$ K, envelope infall rate $\dot{M}_{\text{env}} = 10^{-4} M_{\odot} \text{ yr}^{-1}$, $R_{\text{out}} = 11,000$ AU, Ang = 27 deg, and Incl = 75 deg. The total luminosity and envelope mass of this best-fit model are consistent with our values ($18.4 L_{\odot}$ and $7.4 M_{\odot}$).

Looking at the 10 best-fitting models, only the age ($t < 2 \times 10^5$ yr), protostellar mass ($M_* < 2 M_{\odot}$), temperature ($T_* = 3000\text{--}4500$ K), and envelope infall rate ($\dot{M}_{\text{env}} = 10^{-5}\text{--}10^{-4} M_{\odot} \text{ yr}^{-1}$) are reasonably well constrained, while the other parameters cover a large range. We do not attempt to constrain the disk properties as the SED is relatively insensitive to the disk in embedded sources. In addition, we cannot use the online grid to constrain the envelope inner radius, because it is fixed to the disk inner radius and very few models with both large envelope mass ($> 1 M_{\odot}$) and large inner envelope radius ($\gtrsim 10$ AU) are included in the grid. This difference in the inner envelope behavior likely accounts for the large outer radius and inclination required by the Robitaille et al. (2007) models.

Given our limited exploration of various models, we feel that the Ulrich envelope model provides the best description of the observed SED. While the derived disk parameters do depend on the input envelope density profile, even in the most conservative case $M_{\text{disk}} \gtrsim 0.1 M_{\odot}$.

6. DISCUSSION

Our derived disk mass of $M_{\text{disk}} \sim 1.0 M_{\odot}$ within a radius of 300 AU is consistent with the Brown et al. (2000) limit of $M_{\text{disk}} > 0.1 M_{\odot}$, as well as the Hogerheijde et al. (1999) limit of $0.7 M_{\odot}$ on the unresolved mass within a radius of 100 AU. The early evolutionary state of FIRS 1 is confirmed by the low bolometric temperature ($T_{\text{bol}} \sim 56$ K) and the small disk-to-envelope mass ratio ($M_{\text{disk}}/M_{\text{env}} \sim 0.1$) despite the high disk mass. Thus, our results suggest that large disks can accumulate very early in the protostellar collapse process.

The FIRS 1 disk is likely too small to be considered a magnetically supported “pseudo-disk.” Given the expected young age of FIRS 1, however, both the mass and radius derived here are much larger than expected for disk formation via gravitational collapse of a rotating core. Terebey et al. (1984) predict that the disk radius, where centrifugal balance is achieved, should

depend on the initial rotation Ω and isothermal sound speed c_s in the core as

$$R_d = 7 \left(\frac{c_s}{0.35 \text{ km s}^{-1}} \right) \left(\frac{\Omega}{4 \times 10^{-14} \text{ s}^{-1}} \right)^2 \left(\frac{t}{10^5 \text{ yr}} \right)^3 \text{ AU.} \quad (4)$$

Based on the statistical relationship between T_{bol} and time derived in Enoch et al. (2009; $T_{\text{bol}} \propto t^{1.8}$), the bolometric temperature of FIRS 1 suggests that it has an age of $(0.7\text{--}0.8) \times 10^5$ yr. For a reasonable sound speed, $c_s \sim 0.23 \text{ km s}^{-1}$ ($T \sim 15 \text{ K}$), this age and $R_{\text{disk}} = 300 \text{ AU}$ requires an initial rotation rate of approximately $5 \times 10^{-13} \text{ s}^{-1}$. This value is higher than typical dense cores, which have $\Omega \sim 10^{-13}\text{--}10^{-14} \text{ s}^{-1}$ (Goodman et al. 1993). Alternatively, if the age of the source is actually closer to 3×10^5 yr, a more typical rotation rate would be sufficient for growing a 300 AU disk.

Similarly, we can estimate how long it would take for the disk to build up $1 M_{\odot}$ via infall from the envelope. For an infall rate of $\dot{M}_{\text{env}} \sim c_s^3/G \sim 10^{-5} M_{\odot} \text{ yr}^{-1}$, and conservatively assuming that all of the infalling material falls onto the disk rather than directly onto the protostar, accumulating $1 M_{\odot}$ would take 10^5 yr. Although this is probably close to the age of FIRS 1, a disk of $1 M_{\odot}$ requires that little of the infalling material be accreted from the disk onto the star. Below we mention a few plausible methods for building up a large circumprotostellar disk in this object.

A Class 0 lifetime longer than a few times 10^5 yr, i.e., longer than the estimated timescale for Class 0 sources in nearby low-mass star-forming regions (Enoch et al. 2009; Evans et al. 2009), would allow larger disks to grow before the end of the Class 0 phase.

FIRS 1 may have a higher envelope infall rate than average, allowing the disk to quickly accumulate mass. The bolometric luminosity of FIRS 1 is quite large compared to the typical luminosity of YSOs in nearby low-mass star-forming regions ($\lesssim 1 L_{\odot}$; Dunham et al. 2008; Enoch et al. 2009). A luminosity of $11 L_{\odot}$ implies an accretion rate onto the protostar of at least $2 \times 10^{-5} M_{\odot} \text{ yr}^{-1}$ (for $\dot{M}_* \sim R_* L_{\text{bol}}/GM_*$, $R_* \sim 5 R_{\odot}$ and $M_* \sim 1 M_{\odot}$). If this corresponds to an even higher envelope infall rate, $\dot{M}_{\text{disk}} \sim 1 M_{\odot}$ could easily be achieved in $(0.7\text{--}0.8) \times 10^5$ yr.

If the FIRS 1 disk has very low viscosity, mass may build up in the disk with very little accreting onto the protostar (although this is at odds with the high luminosity). Brown et al. (2000) suggest that early disk formation and similar disk masses in the Class 0 and Class I phases could be achieved with a time-dependent viscosity, low at early times and higher by Class I.

Perhaps more likely, this source could have recently entered a period of relatively rapid accretion, as expected in the episodic accretion scenario (e.g., Hartmann & Kenyon 1985; Enoch et al. 2009; Evans et al. 2009). Such a high mass disk around a presumably low protostar mass should be unstable, and undergoing rapid accretion, explaining the high luminosity. In this picture, the current high accretion phase would have been preceded by a period of low accretion onto the protostar while material built up in the disk (assuming infall from the envelope onto the disk is steady).

A larger sample is certainly needed to determine if such large, high mass disks are typical in the Class 0 phase. The recent Jørgensen et al. (2009) study of 20 Class 0 and Class I sources finds disk masses in Class 0 from $0.01\text{--}0.5 M_{\odot}$, and $M_{\text{disk}}/M_{\text{env}}$ ratios of $1\%\text{--}10\%$. If we calculate our disk mass by the same method as Jørgensen et al. (2009), which uses the flux

at $50 \text{ k}\lambda$ and assumes an optically thin, unresolved disk, we get $M_{\text{disk}} = 0.6 M_{\odot}$. While this is at the high end of the Jørgensen et al. (2009) disk sample, the disk-to-envelope mass ratio ($\sim 8\%$ when using $M_{\text{disk}} = 0.6 M_{\odot}$) is consistent with their results, as is the idea that disks are already well established in the Class 0 stage.

Regarding the envelope structure, it is important to keep in mind that while we refer to R_{cent} as the centrifugal radius, our model is not dynamical, and there is no dependence on rotation rate. Thus the sharp drop in density inside of this radius could have any number of causes, including a companion that has cleared out material, as well as rotational collapse onto a disk. Any binary companion with a disk mass larger than $0.1 M_{\odot}$ should have been detected. There is a tentative second detection 500 AU to the northwest of FIRS 1 (see Figure 3(C)); the peak of approximately 55 mJy would correspond to a disk mass of $\sim 0.06 M_{\odot}$, but this may just be a ‘‘clumpy’’ feature in the envelope. The more likely explanation is that the inner envelope cavity is a result of collapse in a rotating core, and creation of the 300 AU radius disk. Alternatively, a clumpy envelope could cause a similar decrease in MIR opacity and might alleviate the need for an inner envelope hole (Indebetouw et al. 2006).

If the disk and envelope are physically connected, with both the disk and inner envelope hole governed by rotation in the collapsing core, we might expect $R_{\text{disk}} \approx R_{\text{cent}}$. Although the best-fit R_{cent} is a factor of 2 larger than R_{disk} here, the range of reasonable values allow for R_{cent} to be as small as 400 AU and R_{disk} to be as large as 500 AU. Thus, a physical continuity between the disk and envelope is certainly plausible.

7. SUMMARY

We utilize *Spitzer* IRS spectra, high-resolution CARMA 230 GHz continuum data, and broadband photometry together with a grid of radiative transfer models to characterize the disk and envelope structure of the Class 0 protostar Serpens FIRS 1. Our conclusions are the following.

1. Radiative transfer models combined with mid-infrared spectra and millimeter data with excellent uv -coverage can reasonably constrain envelope parameters, including the inner (centrifugal) radius, outer radius, and outflow opening angle. In all cases, there is a range of parameter values able to reasonably fit the data. Once the envelope parameters have been determined, the mass and radius of the disk are robustly constrained by millimeter interferometry data with uv -coverage from <5 to $>300 \text{ k}\lambda$.
2. We find a centrifugal radius for FIRS 1 in the range 400–700 AU, indicating a large ‘‘hole’’ in the inner envelope, similar to IRAS 16293 (Jørgensen et al. 2005b). Unlike IRAS 16293, however, there is no strong evidence for a binary companion that might have cleared out the inner envelope. Other explanations for such a large R_{cent} in this source are: (1) collapse of the inner envelope onto the disk due to the conservation of angular momentum in a rotating, collapsing core; or (2) the R_{cent} does not indicate a true inner radius, but rather a ‘‘clumpy’’ envelope with much lower opacity in the MIR than a smooth envelope density profile.
3. Using envelope parameters set by the SED, the CARMA 230 GHz visibilities require a quite massive, resolved disk. The best-fitting disk has a mass of $1 M_{\odot}$, and a radius of approximately 300 AU. While this mass is consistent with previous limits (Hogerheijde et al. 1999; Brown et al. 2000),

it also indicates that protostars can accumulate relatively massive disks at very early times. This is somewhat at odds with theoretical expectations that disks start small and grow with time (Terebey et al. 1984). The range of reasonable disk and envelope parameters does allow for a physical continuity between the disk and inner envelope.

4. Our results for FIRS 1 demonstrate the feasibility of using this method to characterize the disk and envelope structure in a larger sample of Class 0 sources. Similar modeling for an unbiased sample will allow us to characterize the typical disk mass, size, and inner envelope structure during the Class 0 phase.

The authors thank the referee T. Bourke, and N. Evans for comments and suggestions that improved this manuscript. We are also grateful to C. Dullemond for the use of his RADMC radiative transfer code and helpful discussions, and to A. Crapsi for providing his model setup. Support for this work was provided by NASA through the Spitzer Space Telescope Fellowship Program, through a contract issued by the Jet Propulsion Laboratory (JPL), California Institute of Technology, under a contract with NASA. Support for CARMA construction was derived from the states of California, Illinois, and Maryland, the Gordon and Betty Moore Foundation, the Kenneth T. and Eileen L. Norris Foundation, the Associates of the California Institute of Technology, and the National Science Foundation. Ongoing CARMA development and operations are supported by the National Science Foundation under a cooperative agreement, and by the CARMA partner universities. Support for c2d, a Spitzer Legacy Science Program, was provided by NASA through contracts 1224608 and 1230782 issued by JPL, California Institute of Technology, under NASA contract 1407. The development of Bolocam was provided by NSF grants AST-9980846 and AST-0206158.

REFERENCES

- André, P. 1994, in Proc. 28th Rencontre de Moriond, The Cold Universe, ed. T. Montmerle et al. (Gif-sur-Yvette, France: Editions Frontieres), 179
- Andrews, S. M., & Williams, J. P. 2007, *ApJ*, **671**, 1800
- Brown, D. W., Chandler, C. J., Carlstrom, J. E., Hills, R. E., Lay, O. P., Matthews, B. C., Richer, J. S., & Wilson, C. D. 2000, *MNRAS*, **319**, 154
- Casali, M. M., Eiroa, C., & Duncan, W. D. 1993, *A&A*, **275**, 195
- Chandler, C. J., Koerner, D. W., Sargent, A. I., & Wood, D. O. S. 1995, *ApJ*, **449**, 139
- Chen, H., Myers, P. C., Ladd, E. F., & Wood, D. O. S. 1995, *ApJ*, **445**, 377
- Chiang, E. I., & Goldreich, P. 1997, *ApJ*, **490**, 368
- Crapsi, A., van Dishoeck, E. F., Hogerheijde, M. R., Pontoppidan, K. M., & Dullemond, C. P. 2008, *A&A*, **486**, 245
- Curiel, S., Rodríguez, L. F., Gómez, J. F., Torrelles, J. M., Ho, P. T. P., & Eiroa, C. 1996, *ApJ*, **456**, 677
- Curiel, S., Rodríguez, L. F., Moran, J. M., & Cantó, J. 1993, *ApJ*, **415**, 191
- Davis, C. J., Matthews, H. E., Ray, T. P., Dent, W. R. F., & Richer, J. S. 1999, *MNRAS*, **309**, 141
- Dowell, C. D., et al. 2003, *Proc. SPIE*, **4855**, 73
- Dullemond, C. P., & Dominik, C. 2004, *A&A*, **417**, 159
- Dunham, M. M., Crapsi, A., Evans, N. J., II, Bourke, T. L., Huard, T. L., Myers, P. C., & Kauffmann, J. 2008, *ApJS*, **179**, 249
- Eisner, J. A., Hillenbrand, L. A., Carpenter, J. M., & Wolf, S. 2005, *ApJ*, **635**, 396
- Enoch, M. L., Evans, N. J., II, Sargent, A. I., & Glenn, J. 2009, *ApJ*, **692**, 973
- Enoch, M. L., Glenn, J., Evans, N. J., II, Sargent, A. I., Young, K. E., & Huard, T. L. 2007, *ApJ*, **666**, 982
- Evans, N. J., II, et al. 2003, *PASP*, **115**, 965
- Evans, N. J., II, et al. 2009, *ApJS*, **181**, 321
- Galli, D., & Shu, F. H. 1993, *ApJ*, **417**, 220
- Glenn, J., et al. 2003, *Proc. SPIE*, **4855**, 30
- Goodman, A. A., Benson, P. J., Fuller, G. A., & Myers, P. C. 1993, *ApJ*, **406**, 528
- Hartmann, L., & Kenyon, S. J. 1985, *ApJ*, **299**, 462
- Harvey, D. W. A., Wilner, D. J., Lada, C. J., Myers, P. C., & Alves, J. F. 2003, *ApJ*, **596**, 383
- Harvey, P. M., Wilking, B. A., & Joy, M. 1984, *ApJ*, **278**, 156
- Harvey, P. M., et al. 2006, *ApJ*, **644**, 307
- Harvey, P. M., et al. 2007, *ApJ*, **663**, 1139
- Hatchell, J., Fuller, G. A., Richer, J. S., Harries, T. J., & Ladd, E. F. 2007a, *A&A*, **468**, 1009
- Hogerheijde, M. R., van Dishoeck, E. F., & Salverda, J. M. 1999, *ApJ*, **513**, 350
- Houck, J., et al. 2004, *ApJS*, **154**, 18
- Hurt, R. L., & Barsony, M. 1996, *ApJ*, **460**, L45
- Indebetouw, R., Whitney, B. A., Johnson, K. E., & Wood, K. 2006, *ApJ*, **636**, 362
- Jørgensen, J. K., Bourke, T. L., Myers, P. C., Schöier, F. L., van Dishoeck, E. F., & Wilner, D. J. 2005a, *ApJ*, **632**, 973
- Jørgensen, J. K., Johnstone, D., Kirk, H., & Myers, P. C. 2007, *ApJ*, **656**, 293
- Jørgensen, J. K., Johnstone, D., Kirk, H., Myers, P. C., Allen, L. E., & Shirley, Y. L. 2008, *ApJ*, **683**, 822
- Jørgensen, J. K., van Dishoeck, E. F., Visser, R., Bourke, T. L., Wilner, D. J., Lommen, D., Hogerheijde, M. R., & Myers, P. C. 2009, *A&A*, in press (arXiv:0909.3386)
- Jørgensen, J. K., et al. 2005b, *ApJ*, **631**, L77
- Lahuis, F., et al. 2006, c2d Spectroscopy Explanatory Suppl. (Pasadena, CA: Spitzer Science Center)
- Larsson, B., et al. 2000, *A&A*, **363**, 253
- Looney, L. W., Mundy, L. G., & Welch, W. J. 2000, *ApJ*, **529**, 477
- Moscadelli, L., Testi, L., Furuya, R. S., Goddi, C., Claussen, M., Kitamura, Y., & Wootten, A. 2006, *A&A*, **446**, 985
- Myers, P. C., & Ladd, E. F. 1993, *ApJ*, **413**, 47
- Ossenkopf, V., & Henning, Th. 1994, *A&A*, **291**, 943
- Robitaille, T. P., Whitney, B. A., Indebetouw, R., & Wood, K. 2007, *ApJS*, **169**, 328
- Robitaille, T. P., Whitney, B. A., Indebetouw, R., Wood, K., & Denzmore, P. 2006, *ApJS*, **167**, 256
- Rodríguez, L. F., Curiel, S., Moran, J. M., Mirabel, I. F., Roth, M., & Garay, G. 1989, *ApJ*, **346**, L85
- Sault, R. J., Teuben, P. J., & Wright, M. C. H. 1995, in ASP Conf. Ser. 77, Astronomical Data Analysis Software and Systems IV, ed. R. A. Shaw, H. E. Payne, & J. J. E. Hayes (San Francisco, CA: ASP), **433**
- Steer, D. G., Dewdney, P. E., & Ito, M. R. 1984, *A&A*, **137**, 159
- Straizys, V., Cernis, K., & Bartasiute, S. 1996, *Baltic Astron.*, **5**, 125
- Terebey, S., Shu, F. H., & Cassen, P. 1984, *ApJ*, **286**, 529
- Testi, L., & Sargent, A. I. 1998, *ApJ*, **508**, L94
- Ulrich, B. T., Neugebauer, G., McCammon, D., Leighton, R. B., Hughes, E. E., & Becklin, E. 1967, *ApJ*, **147**, 858
- Werner, M., et al. 2004, *ApJS*, **154**, 1
- Wolf, S., Padgett, D. L., & Stapelfeldt, K. R. 2003, *ApJ*, **588**, 373